HHS Public Access

Author manuscript

Cell. Author manuscript; available in PMC 2022 September 30.

Published in final edited form as:

Cell. 2021 September 30; 184(20): 5151–5162.e11. doi:10.1016/j.cell.2021.08.021.

Open State Structure and Pore Gating Mechanism of the Cardiac Sodium Channel

Daohua Jiang[1,2], **Richard Banh**[3], **Tamer M. Gamal El-Din**[1], **Lige Tonggu**[1], **Michael Lenaeus**[1,4], **Régis Pomès**[3], **Ning Zheng**[*,1,5], **William A. Catterall**[*,1]

[1]Department of Pharmacology, University of Washington, Seattle, WA 98195;

[2]Laboratory of Soft Matter Physics, Institute of Physics, Chinese Academy of Sciences, Beijing 100190, China;

[3]Molecular Medicine, Hospital for Sick Children, Toronto, ON, Canada M5G 0A4 and Department of Biochemistry, University of Toronto, Toronto, ON, Canada M5S 1A8;

[4]Division of General Internal Medicine, Department of Medicine, University of Washington, Seattle, WA 98195;

[5]Howard Hughes Medical Institute, University of Washington, Seattle, WA 98195

SUMMARY

The heartbeat is initiated by voltage-gated sodium channel $Na_V1.5$, which opens rapidly and triggers the cardiac action potential; however, the structural basis for pore opening remains unknown. Here we blocked fast inactivation with a mutation and captured the elusive open-state structure. The fast-inactivation gate moves away from its receptor, allowing asymmetric opening of pore-lining S6 segments, which bend and rotate at their intracellular ends to dilate the activation gate to ~10Å diameter. Molecular-dynamics analyses predict physiological rates of Na^+ conductance. The open-state pore blocker propafenone binds in a high-affinity pose, and drug-access pathways are revealed through the open activation gate and fenestrations. Comparison with mutagenesis results provides a structural map of arrhythmia mutations that target the activation and fast inactivation gates. These results give atomic-level insights into molecular events that underlie generation of the action potential, open-state drug block, and fast inactivation of cardiac sodium channels, which initiate the heartbeat.

Graphical Abstract

Corresponding Authors: William A. Catterall, wcatt@uw.edu, Ning Zheng, nzheng@uw.edu, Daohua Jiang, jiangdh@iphy.ac.cn.
*Co-Senior Authors
Lead Contact: William A. Catterall, wcatt@uw.edu

AUTHOR CONTRIBUTIONS

D. J., R. B., T. M. G., L. T., M. L., R. P., N. Z., and W. A. C. designed the experiments; D. J., R. B., T. M. G., L. T., and M. L performed the experiments; D. J., R. B., T. M. G., R. P., N. Z., and W. A. C. wrote the manuscript; and all authors revised and edited the manuscript.

DECLARATION OF INTEREST

The authors declare no competing interests.

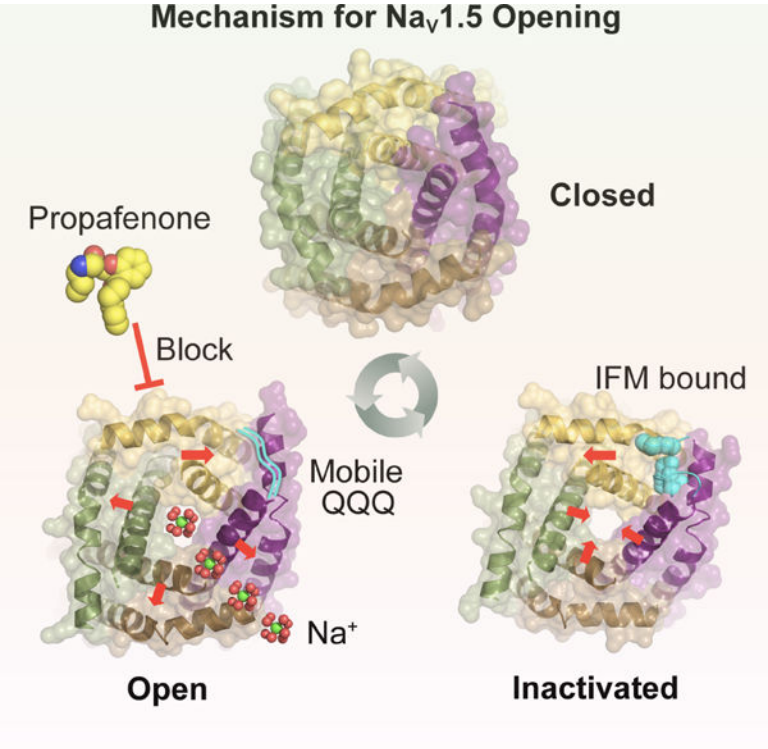

In Brief

Using a mutation to block fast sodium channel inactivation, the open-state structure of the primary cardiac sodium channel Na$_V$1.5 was captured, revealing the molecular mechanisms for rapid opening and fast inactivation of the pore as well as the receptor site for high-affinity binding of the open-state sodium channel blocker propafenone.

INTRODUCTION

The voltage-gated sodium channel Na$_V$1.5 activates in less than 1 millisecond to trigger the cardiac action potential and inactivates within 2–3 milliseconds to allow repolarization and return to the resting state in preparation for firing the next action potential (reviewed in (Catterall and Maier, 2015; Noble, 1984)). How these physiologically essential conformational transitions open and close the pore at this rapid rate remains unknown. Mutations of Na$_V$1.5 cause life-threatening cardiac arrhythmias (Clancy and Kass, 2005). Class I sodium channel-blocking antiarrhythmic drugs block Na$_V$1.5 by binding to a receptor site in the pore (Catterall et al., 2020; Hille, 2001; Hondeghem and Katzung, 1984). By solving the structure of Na$_V$1.5 in the open state and comparing that structure with those of the resting and inactivated states, we reveal the mechanisms of rapid opening and fast inactivation of the pore at atomic resolution and show how these processes are modified by antiarrhythmic drugs and arrhythmia mutations.

Eukaryotic Na$_V$s are composed of a large pore-forming α subunit and smaller auxiliary β-subunits (Ahern et al., 2016; Catterall, 2000). The α-subunit contains 24 transmembrane

segments organized in four homologous domains (*D*I-*D*IV). The first four segments of each domain (S1-S4) comprise the voltage sensors (VS), and the S5 and S6 segments and the pore loop between them (S5-P-S6) form the pore module (PM). The intracellular ends of the pore-lining S6 segments serve as the activation gate, which rapidly opens the pore, and the intracellular loop connecting *DIII* and *DIV* (L_{III-IV}) forms the fast inactivation gate, which closes the pore (Catterall, 2000; Goldin, 2003). Mutation of a triple-hydrophobic motif in L_{III-IV}, Ile-Phe-Met (IFM), completely eliminates fast inactivation (Goldin, 2003; West et al., 1992). Structures of Na_Vs from prokaryotes, nerve, skeletal muscle, and heart reveal a conserved transmembrane core (Jiang et al., 2020; Pan et al., 2018; Payandeh et al., 2011; Shen et al., 2019). However, in all mammalian Na_V structures, the pore is closed by the activation gate at the intracellular ends of the S6 segments and inactivated by binding of the fast inactivation gate. Capturing the open state is challenging because it remains open for only 1–2 milliseconds before the fast inactivation gate closes and blocks it. Therefore, the structure of the open state and the mechanism of pore opening of the mammalian Na_V channels remain unknown. Here we introduced the mutation IFM/QQQ into the fast inactivation gate to block fast inactivation, successfully captured the structure of the resulting open state at high resolution by cryo-EM, and revealed the structural mechanisms for rapid opening, fast inactivation, and open-state block in atomic detail.

RESULTS AND DISCUSSION

Capturing $Na_V1.5$ in the Open State

The inward sodium current conducted by $Na_V1.5$ activates and inactivates within 2–3 milliseconds (Figure 1A; drawn downward by convention). In contrast, $Na_V1.5$/QQQ opens but does not inactivate (Figure 1B), even though its voltage dependence of activation is unchanged (Figure 1C). High expression of $Na_V1.5$/QQQ is cytotoxic due to continuous leak of Na^+. However, $Na_V1.5$/QQQ can be blocked by the Class IC antiarrhythmic drug propafenone (Kohlhardt and Fichtner, 1988), which enters the open pore and blocks the inward Na^+ current during single depolarizations (Figure 1D, top). Importantly, propafenone does not block $Na_V1.5$ in the resting state at the holding potential; however, as the inward sodium current approaches its maximum, propafenone enters the pore and blocks the open state (Fig. 1D, red). As expected for open-state block (Kohlhardt and Fichtner, 1988), repetitive stimulation increased drug inhibition, which was also more prominent at higher drug concentrations (Figure 1D, bottom; Figure 1E). Use-dependent block during rapid stimulation was more potent than block at a low rate of stimulation or block with no prior stimulation (Figure 1F).

Guided by these observations, we expressed $Na_V1.5$/QQQ trapped in the open state at a high level in the presence of propafenone in order to stabilize the open state structure and prevent pathogenic leak of Na^+ into the transfected cells (STAR Methods). The mutant channel was solubilized, purified, and analyzed at high resolution by cryo-EM (STAR Methods; Figures S1-S3 (Jiang et al., 2020)). The four domains of $Na_V1.5$/QQQ are organized in a domain-swapped manner, and the overall core structure has a root mean square deviation (RMSD) of 1.04 Å over 1127 C-α residues compared to $Na_V1.5$ (Figure 2A and B; Figure S4; (Jiang et al., 2020)). The selectivity filter, the four voltage sensors, and the pore-lining

S6 segments are well fit by the cryo-EM density and are very similar to $Na_V1.5$ (Figure 2A and B; Figure S4). In contrast, there are major conformational changes in the activation gate, the fast inactivation gate, and its receptor, highlighting the critical role of these highly localized structural transitions in rapid opening and closing of the pore.

Releasing the Fast Inactivation Gate of $Na_V1.5$/QQQ

Voltage-gated sodium channels are purified in the inactivated state, which is the most stable state at 0 mV. In previous structures of mammalian Na_V channels, the fast inactivation gate has been closed and the IFM motif has been inserted into its receptor in a hydrophobic pocket between the intracellular end of the S6 segment and the S4-S5 linker in *D*IV, as illustrated for wildtype $Na_V1.5c$ in Figure 2C and D. This position of the fast inactivation gate holds the pore closed; therefore, the fast inactivation gate must be released before the pore can open. In our native $Na_V1.5c$ structures, the complete length of the intracellular linker connecting *D*III and *D*IV is clearly resolved and has robust cryo-EM density (Figure 2C and D, right), including the IFM motif of the fast inactivation gate (Figure 2D, right, circle). In contrast, there are striking changes in the conformations of the fast inactivation gate and its receptor in $Na_V1.5$/QQQ (Figure 2A, C, and D). We did not observe any cryo-EM density for the QQQ region of the fast inactivation gate (Leu1482-Met1489) (Figure 2A and C; dotted lines). Close inspection reveals that the cryo-EM density representing the linker connecting *D*III and *D*IV is narrow and discontinuous compared to native $Na_V1.5c$ (Figure 2D), and the hydrophobic pocket that binds the IFM motif is empty in $Na_V1.5$/QQQ (Figure 2C and D, circles). Evidently, loss of IFM binding to the hydrophobic pocket in the inactivation gate receptor destabilizes the interaction between the *D*III-*D*IV loop and the *D*IV S4-S5 linker helix, and the increased mobility of the *D*III-*D*IV linker releases the fast inactivation gate to adopt a flexible conformation that renders it invisible in cryo-EM. It is remarkable that the dramatic functional effect of the IFM/QQQ mutation in completely blocking fast inactivation (Figure 1A and B) results from these local conformational changes in the fast inactivation gate, the IFM motif, and its receptor, without inducing major conformational change in the transmembrane core. These results focus attention on this small region of $Na_V1.5$ as the primary mediator of pore gating and fast inactivation. These local conformational changes may have evolved to provide rapid and precise opening and closing of the activation gate, which takes place in less than 100 μsec under physiological conditions (Benndorf, 1994).

Opening the Activation Gate of $Na_V1.5$/QQQ

Even though there was little overall change in the structure of $Na_V1.5$/QQQ, we observed marked helical shifts in the S6 segments that form the intracellular activation gate (Figure 3A and B). The S6 segments move outward from the pore axis to enlarge the orifice of the activation gate. The bends of the four S6 segments start at the middle of each helix and are maximal at the intracellular ends (Figure 3A and B). Ser1460 and Ser1761 serve as the starting points for bending of *D*III S6 and *D*IV S6, respectively (Figure 3B). Strikingly, the movements of the S6 segments in *D*III (2.3 Å) and *D*IV (6.1 Å) are much larger than the movements of the S6 segments in *D*I or *D*II (Figure 3A and B). *DIV*-S6 shifts directly toward the IFM receptor and compresses its binding pocket by >2 Å (Figure 3C and D). This movement expels the IFM motif from its receptor and releases the fast inactivation gate.

Previous mammalian Na_V structures in inactivated states indicated that the IFM motif in the fast inactivation gate folds into the pore module, as proposed in the 'hinged-lid' model of fast inactivation (Catterall, 2000), and prevents opening of the activation gate through local allosteric interactions (Jiang et al., 2020; Pan et al., 2018; Shen et al., 2019). In our $Na_V1.5$/QQQ structure, binding of the hydrophilic QQQ motif to the hydrophobic pocket in the inactivation gate receptor is unfavorable, leaving this motif mobile in the cytosol and invisible to cryo-EM. Consequently, *D*IV-S6 moves away from the pore axis, occupies the space that previously accommodated the IFM motif, and allows opening of the activation gate.

Structure of the Open Activation Gate

The movements of *D*III S6 and *D*IV S6 that open the pore are illustrated in three dimensions in Figure 3C-E. *D*III S6 of $Na_V1.5$/QQQ moves modestly away from the pore axis, whereas *D*IV S6 moves substantially further away (Figure 3C and D, red). The 6.1 Å movement of *D*IV S6 creates a clash with the bound IFM motif of the inactivation gate and pushes it out of its receptor site (Figure 3C and D, red). These movements open the orifice of the pore to an average diameter of ~10 Å, as measured at the centers of the distal carbon atoms of the surrounding amino acid side chains (Figure 3E). The side chains of the amino acids in the four S6 segments of $Na_V1.5$ that close the pore are asymmetric, with a short Ala side chain in *D*I compared to Ile and Leu residues in the other three domains (Figure 3E). This structure results in an asymmetric orifice of the activation gate, with Cα distances of 10.6 Å between *D*II and *D*IV and 9.7 Å between *D*I and *D*III (Figure 3E).

The series of state-dependent conformational changes that are implied by our structures are illustrated in Figure 4A-C. In our model of the resting state (Jiang et al., 2020; Wisedchaisri et al., 2019), the side chains of hydrophobic residues in the S6 segments nearly completely close the orifice of the activation gate (Figure 4A). Strikingly, in the open state described here, bending and twisting motions of the S6 segments move those side chains out of the ion conductance pathway and open the pore (Figure 4B). For example, the side chain of V413 is twisted out of the lumen of the pore and is replaced in the pore lining by A414, the side chain of I1471 is moved out of the lumen and is partially replaced by I1472, and the side chains of both L941 and I1773 are pulled away from the pore axis in the open state (Figure 4A and B). In contrast, in the fast-inactivated states characterized previously (Jiang et al., 2020; Pan et al., 2018; Shen et al., 2019), the IFM motif of the inactivation gate is bound in its receptor, the orifice of the intracellular activation gate is narrowed by movements of the S6 segments, most notably *D*III S6 and *D*IV S6, and the activation gate is functionally closed (Figure 4C). The open state structure of Na_VAb, an ancestral homotetrameric Na_V channel, has a four-fold symmetric orifice of ~10 Å (Lenaeus et al., 2017). The four S6 segments of $Na_V1.5$/QQQ open to a similar average diameter (Figure 3E), suggesting that $Na_V1.5$/QQQ was successfully captured in its open state.

Sodium channels conduct Na^+ as a hydrated cation (Hille, 2001). To further illustrate the potential functional properties of this open-state structure, we constructed van der Waals space-filling models to compare the size of the orifice of the activation gate in resting, open, and inactivated states to the size of hydrated Na^+, whose diameter is 7.2 Å. Hydrated Na^+

fits through the orifice in the open state with little room to spare (Figure 4E; see legend for van der Waals measurements). In contrast, the orifice of the activation gate is too small to accommodate hydrated Na^+ in the resting or inactivated states (Figure 4D, F). To support this point further, we cut sections through the center of $Na_V1.5$ in the inactivated and open states and illustrated the side views of the van der Waals surfaces (Figure 5A, B, D, E). In the open state, the pathway from the central cavity to the cytosol through the activation gate is wide enough to accommodate hydrated Na^+. In contrast, the orifice of the activation gate is too small to accommodate hydrated Na^+ in the inactivated state. Together, the bottom and side views presented in Figures 4D-F and 5A, B, D, and E show that the relatively small movements of the activation gate revealed by our structures as the sodium channel transitions from closed, to open, to inactivated states are sufficient to provide an all-or-none functional switch controlling the conductance of the open and closed pore. These small conformational movements are consistent with the rapid gating of $Na_V1.5$, in which pore opening and closing takes place in <100 μs under physiological conditions (Benndorf, 1994) in order to precisely trigger and rapidly conduct the cardiac action potential.

Analysis of Na^+ Conductance through the Open Activation Gate by Molecular Dynamics

To further test the hypothesis that our $Na_V1.5$/QQQ structure represents a functionally open state, we carried out molecular dynamics (MD) simulations of $Na_V1.5$ (Jiang et al., 2020), $Na_V1.5$/LqhIII (Jiang et al., 2021), and $Na_V1.5$/QQQ in the presence of harmonic restraints to stabilize the open-state structure (Figure 6; STAR Methods; Figure S5). Water and cations rapidly occupied the selectivity filter and central cavity of the pore in all three $Na_V1.5$ structures. Hydration of the activation gate (*Nwater*) was ~5 for $Na_V1.5$ and ~4 for $Na_V1.5$/LqhIII (Figure 6A, z=−2 nm). In contrast, *Nwater* in $Na_V1.5$/QQQ increased and became bimodal, with two states of comparable populations: a partially dehydrated state with *Nwater* ~8 and a hydrated state with *Nwater* ~18 (Figure 6A, z=−2 nm; Figure 6B and C; Tables S2 and S3), similar to the open state of Na_VAb/1–226, where *Nwater* = 15.1 ± 0.8 (Lenaeus et al., 2017). Importantly, seven spontaneous Na^+ translocation events across the open activation gate occurred in 5 μs of simulation (median, 10,000 bootstraps with replacement, sample size = 50 replicas of 100 ns, IQR = 5–9; Figure 6D; Figure S6). In contrast, identical simulations for 6.6 μs with native $Na_V1.5c$ and for 5 μs with $Na_V1.5c$/LqhIII did not reveal any Na^+ permeation events. Because only ~½ of individual channels are hydrated and conductive simultaneously (Figure 6C, Tables S2 and S3), the frequency of ion transit per open channel is ~2.8 per μsec (IQR = 2.0–3.6). The single channel conductance of sodium channels is ~10–20 pS (eg., (Weiss and Horn, 1986)), commensurate with single ion transit rates of ~4–8 per μsec. Thus, these results further validate the structure of the open, functionally conductive activation gate at atomic resolution.

The open state of $Na_V1.5$ is inherently unstable, with a half-life of <50 μsec under physiological conditions (Benndorf, 1994). Unrestrained MD simulations revealed pore contraction, resulting in asymmetric conformations with $d2 < d1$ (Figure S5, top). The activation gate of unrestrained $Na_V1.5$/QQQ was slightly more hydrated, but Na^+ never passed through it (Figure 6; Figure S6). This instability of the open state in our MD model may be correlated with the short half-life of the open state of the pore under physiological conditions (Benndorf, 1994). Consistent with the mechanism of hydrophobic gating found in

many ion channels (Aryal et al., 2015; Neale et al., 2015), a small increase in the diameter of the activation gate of $Na_V1.5$/QQQ was sufficient to drive the wetted-dewetted equilibrium toward the hydrated state of the gate and permit Na^+ translocation (Figure 6C; Table S2).

Receptor Site for Open State Block by Propafenone

The Class 1C antiarrhythmic drug propafenone blocks open $Na_V1.5$ channels with high affinity (Kohlhardt and Fichtner, 1988). Clinical use of propafenone relies on state-dependent binding to open and/or inactivated $Na_V1.5$ channels, which targets its inhibitory effects to depolarized, rapidly firing cardiac myocytes that drive life-threatening arrhythmias (Catterall et al., 2020). Consistent with this mechanism, propafenone blocked $Na_V1.5$/QQQ during single long test pulses, and its block accumulated in trains of pulses in a concentration-dependent manner (Figure 1D-F). Propafenone did not have any effect on the sodium current at the holding potential, indicating that it cannot block the $Na_V1.5$ channel in the resting state, even when inactivation is prevented by the IFM/QQQ mutation (Figure 1D). Only after the pore opens and the inward sodium current approaches its peak, can propafenone enter the pore through the open activation gate (as modeled in Figure 5C and F) and block Na^+ conductance, eventually reducing it to ~50% of maximum at steady state with 10 μM drug. Propafenone binds to the antiarrhythmic drug receptor site in the open pore of $Na_V1.5$/QQQ, physically blocking the exit of ions from the ion selectivity filter into the central cavity (Figure 7A and B) but leaving the intracellular activation gate open for entry of drug from the cytosol (Figure 7C). The open state of the activation gate is wide enough to accommodate an entering propafenone molecule, whereas the inactivated state is too narrow, as modeled in Figure 5C and F. The binding position of propafenone is consistent with high-affinity drug block because its two aromatic rings reach toward the walls of the central cavity to interact with F1762 and Y1769 (Figure 7D-F), which form high-affinity interactions with bound antiarrhythmic drugs (Pless et al., 2011; Ragsdale et al., 1994). Drug binding is stabilized by a π-π stacking interaction with this state-dependent binding pose of propafenone (4.7 Å, Figure 7E and F) and by on-edge van der Waals interactions with Y1769 (Figure 7E). Bound propafenone also interacts with Q372 in the pore helix in *D*I, which has not previously been implicated in drug binding (Figure 7E and F). Its positively charged amino group is located in an ideal blocking position at the negatively charged exit from the ion selectivity filter, which would prevent the exit of cations into the central cavity (Figure 7C-F). This high-resolution structural information may provide a useful guide to discovery of next-generation antiarrhythmic drugs that are safer and more effective.

Fenestrations and Drug Binding

The structures of voltage-gated sodium channels revealed fenestrations leading from the lipid bilayer into the central cavity (Catterall et al., 2020; Jiang et al., 2020; Pan et al., 2019; Pan et al., 2018; Payandeh et al., 2011), which could provide access for local anesthetic and antiarrhythmic drugs to their receptor site in the resting state (Catterall et al., 2020), as suggested from studies of state-dependent drug block of sodium channels in the modulated receptor hypothesis (Hille, 1977). MD studies support drug access, binding, and block via this route (Boiteux et al., 2014a; Boiteux et al., 2014b; Nguyen et al., 2019). In structure-function studies, we found that reducing the size of fenestrations of Na_VAb

by mutation of a capping residue reduced resting-state drug block, whereas increasing the size of the fenestrations increased resting-state block (Gamal El-Din et al., 2018). Moreover, the changes in resting-state block caused by mutations were correlated with the size of the drug molecule (Gamal El-Din et al., 2018). Thus, propafenone may reach the high-affinity binding pose revealed here (Figure 7) by passing through the fenestrations revealed in $Na_V1.5$ (Catterall et al., 2020; Jiang et al., 2020) in the resting state or by entering through the open activation gate in the open state as shown here (Figure 7C, F (Catterall et al., 2020)). Our structures suggest that drug access through the fenestrations is domain-dependent, because the size and conformation of the fenestrations differ at the four domain interfaces (Figure 7G). Evidently, the extent of use-dependent block is controlled by the ratio of drug entry via two distinct molecular pathways, the open activation gate and the fenestrations, whose transitions are both domain-dependent and state-dependent.

A Structural Map of Fast Inactivation and Pore Gating

Fast inactivation of sodium channels has been extensively studied by site-directed mutagenesis (Catterall, 2000; Goldin, 2003). Site-directed antibodies (Vassilev et al., 1989; Vassilev et al., 1988) and site-directed cleavage of the sodium channel α subunit between homologous domains (Stuhmer et al., 1989) identified the short intracellular loop between *D*III and *D*IV as the lead candidate for the classically defined fast inactivation gate. Consistent with this idea, depolarization to close and hide the fast inactivation gate prevented site-directed antibody modification of the inactivation process (Vassilev et al., 1989; Vassilev et al., 1988). More detailed mutagenesis studies revealed the IFM motif, which serves as the hydrophobic latch of the inactivation gate, and led to proposal of a ‘hinged-lid’ mechanism of fast inactivation in which those residues fold into the intracellular mouth of the pore module and bind there (Kellenberger et al., 1996; Kellenberger et al., 1997a; Kellenberger et al., 1997b; West et al., 1992). Peptides containing the IFM motif were shown to reconstitute fast inactivation in mutant sodium channels (Eaholtz et al., 1994), and measurements of accessibility of the IFM motif using the substituted cysteine accessibility method (Karlin and Akabas, 1998) showed that this amino acid sequence is buried during the fast inactivation process (Kellenberger et al., 1996). A pair of Gly residues serves as a hinge to enable folding of the inactivation gate into its receptor, as assessed from single channel recordings of open-channel lifetimes (Kellenberger et al., 1997a), and the interacting residues that form the functional inactivation gate receptor were extensively mapped to the S4-S5 linkers in Domains III and IV and the intracellular end of the S6 segment in Domain IV (Lerche et al., 1997; McPhee et al., 1998; McPhee et al., 1994, 1995; Smith and Goldin, 1997). The movements of the fast inactivation gate implied by these structure-function studies are consistent with the ‘hinged-lid’ mechanism of fast inactivation (Kellenberger et al., 1996; Kellenberger et al., 1997a; Kellenberger et al., 1997b; West et al., 1992). NMR analysis of the fast inactivation gate in solution revealed the structure of the IFM motif and an adjacent alpha helix in the unbound ‘not-inactivated’ conformation, providing a potential structural model for the open fast inactivation gate (Rohl et al., 1999). These results show clearly how the fast inactivation gate prevents pore opening when it is in its closed position and why recovery from fast inactivation is required for pore opening.

Our current results reveal the structural basis for the allosteric coupling of release of the fast inactivation gate and voltage-dependent pore opening in three dimensions. Release of the IFM motif from its receptor unlocks the bending and twisting movements of the S6 segments in *D*III and *D*IV that are required for pore opening. Although all four S6 segments move away from the pore axis in the activation process, the movements of the S6 segments in *D*III and *D*IV are largest and likely to be the rate-limiting steps for the activation process. Consistent with this idea, measurements of outward gating charge movements by voltage clamp fluorometry reveal that the S4 segments in *D*I and *D*II move first during the activation process, and the S4 segments in *D*III and *D*IV move more slowly and couple activation to fast inactivation (Capes et al., 2013; Chanda and Bezanilla, 2002). This conformational coupling is blocked by α-scorpion toxins, which bind to a receptor site on the S3-S4 linker in *D*IV (Clairfeuille et al., 2019; Jiang et al., 2021; Rogers et al., 1996). As we have shown here, the movements of the S4 segments in the voltage sensors are coupled to pore opening through conformational changes of the S4-S5 linkers in each domain, which serve as a corral in the resting state to immobilize the S6 segments that form the activation gate and then to trigger their movements away from the pore axis during activation and pore opening (Figure 4A-C; (Jiang et al., 2020; Wisedchaisri et al., 2019)). This intricate coupled series of local conformational changes (Figure 4A-C) is the key control mechanism governing both pore opening and fast inactivation on the rapid timescale required for triggering and conducting the cardiac action potential.

Arrhythmia Mutations that Target the Activation and Inactivation Gates

Long QT Syndrome Type-3 (LQT-3) mutations impair fast inactivation and generate arrhythmic sodium currents (Clancy and Kass, 2005). They target the fast inactivation gate, the S4-S5 linkers in *D*III and *D*IV that form the inactivation gate receptor, and the intracellular ends of the S6 segments that form the activation gate (Figure 4G-H, green spheres). Affected amino acid residues include F1488, M1489, and T1490 in the canonical IFMT motif in the fast inactivation gate and its interacting partners in the inactivation gate receptor (Figure 4G-H; (Catterall, 2000)). Strikingly, most of these affected amino acid residues move during pore opening and/or fast inactivation (compare Figure 4A-C with Figure 4G-H). These mutations cause a gain of function by impairing the intrinsic fast inactivation process and producing persistent and repetitive sodium currents that generate arrhythmias. Our results place these life-threatening arrhythmia mutations in three-dimensional context in these crucial functional components of $Na_V1.5$.

Structural Basis for Initiation of the Heartbeat at the Atomic Level

Conductance through the pore of Na_V channels is controlled by two key processes that are essential for action potential generation: rapid opening of the intracellular activation gate followed by rapid closure and inactivation of the pore by the fast inactivation gate. Our results define the mechanisms of these two crucial processes at the atomic level. Subtle bending and twisting motions of the S6 segments, particularly in Domains III and IV, open the fast inactivation gate to an orifice of 10.6 Å x 9.7 Å, allowing rapid entry of Na^+. Importantly, this bending and twisting motion of the S6 segments and opening of the pore occur *before* the binding of propafenone, which locks the activation gate and stabilizes the *bona fide* open state by its binding. In the open state, the fast inactivation gate and its IFM

motif are initially in the cytosol, but this 'hinged lid' immediately swings inward and binds rapidly to the pore module to close the pore within 2–3 milliseconds through local allosteric interactions. These results reveal at the atomic level how the pore opens rapidly, the fast inactivation gate binds almost immediately to close the pore and prevent its re-opening, and the slower recovery from fast inactivation allows the next pore opening to generate a new action potential and sustain the rhythm of the heartbeat.

Limitations of this Study

Although we have validated the functionality of the $Na_V1.5$ construct we used to determine the open state structure, it is not an intact channel, and the protein was purified in the presence of a detergent and was not embedded in a phospholipid bilayer. While the resolution of the structure is high enough for us to resolve small conformational changes at the activation gate, an even higher resolution would help reveal more details of the structural changes, including rotamers of side chains and solvent bound to the protein. Finally, due to technical reasons, we used the open-state blocker propafenone to stabilize the open state of the channel, which could modify the subtle dynamic nature of the open state in the absence of the drug.

STAR METHODS

RESOURCE AVAILABILITY

Lead Contact—Further information and requests for resources and reagents should be directed to and will be fulfilled by the Lead Contact, William A. Catterall (wcatt@uw.edu).

Materials Availability—All unique/stable reagents generated in this study are available from the Lead Contact with a completed Materials Transfer Agreement.

Data and Code Availability—Structural results are available from the Protein Data Bank and the EMData Resource. Other data and code are available upon request to the Lead Contact.

EXPERIMENTAL MODEL AND SUBJECT DETAILS

Microbe strains—*E. coli* GC10 was cultured at 37°C in LB medium supplemented with 100μg/ml of ampicillin for plasmid DNA extraction. *E. coli* DH10Bac was cultured at 37°C in LB medium supplemented with 50 μg/mL kanamycin sulfate, 7 μg/mL gentamicin and 10 μg/mL tetracycline for bacmid production.

Cell lines—Sf9 (*Spodoptera frugiperda*) insect cells were maintained in Grace's Insect Medium and supplemented with 10% FBS and penicillin/streptomycin at 27°C and passaged at 90% confluence for baculovirus production. HEK293S GnTI$^-$ (*Homo sapiens*) mammalian cells were maintained and infected in Dulbecco's Modified Eagle Medium (DMEM) supplemented with 10% FBS and glutamine/penicillin/streptomycin at 37°C and 5% CO_2 for electrophysiology.

Determination of the Cryo-EM Structure of $Na_V1.5$/QQQ—Mammalian Na_Vs are large and structurally complicated transmembrane proteins, which are difficult to express in heterologous cells and purify to homogeneity. We previously overcame these difficulties by developing a fully functional core-construct of $Na_V1.5$ with truncations of unstructured regions of the intracellular loops and C-terminal domain ($Na_V1.5_C$) (Jiang et al., 2020). The IFM/QQQ mutation was introduced into this well-behaved protein construct. As expected from previous work (West et al., 1992), this mutation completely blocked fast inactivation with no effect on the voltage dependence of activation (Figure 1, A-C). However, because the mutation abolishes fast inactivation, HEK293S cells were killed by the constant leak of Na^+ current after two days of over-expression of $Na_V1.5$/QQQ. We optimized expression conditions by testing several Na_V channel blockers, and we finally maintained the HEK293S cells long enough for effective protein expression in the presence of the Na_V-blocking antiarrhythmic drug propafenone (Figure 1D-F). The $Na_V1.5$/QQQ protein was solubilized in detergents and purified in a mono-disperse peak from size-exclusion chromatography (Figure S1A). Despite low yield, cryo-EM micrographs of the concentrated sample showed excellent quality, and the collected micrographs yielded sharp 2D averages with obvious Na_V features (Figure S1B). A total of 287,306 particles were selected for calculating the final reconstruction map (Figures S2 and S3A), which fit the gold-standard Fourier Shell Correlation (FSC) curve at the criterion value of 0.143 with a resolution of 3.3 Å (Figure S3B). A local resolution map revealed the core region of $Na_V1.5$/QQQ at 3.0–3.5 Å (Figure S3A), illustrating the high quality of the cryo-EM map. Cryo-EM density is well distributed in spherical space, and an FSC curve comparing our model to the original cryo-EM map has overall resolution of 3.4 Å (Figure S3C, D).

METHOD DETAILS

Electrophysiology—All experiments were performed at room temperature (21–24°C) as described previously (Jiang et al., 2020). Human HEK293S GnTI$^-$ cells were maintained and infected on cell culture plates in Dulbecco's Modified Eagle's Medium (DMEM) supplemented with 10% FBS and glutamine/penicillin/streptomycin at 37°C and 5% CO_2 for electrophysiology. Unless otherwise mentioned, HEK293S GnTI$^-$ cells were held at −120 mV and 100-ms pulses were applied in 10 mV increments from −120 mV to +60 mV. A P/−4 holding leak potential was set to −120 mV. Extracellular solution contained in mM: 140 NaCl, 2 $CaCl_2$, 2 $MgCl_2$, 10 HEPES, pH 7.4. Intracellular solution contained: 35 NaCl, 105 CsF, 10 EGTA, 10 HEPES, pH 7.4. Glass electrodes had a resistance 1.5–3 MΩ. Currents resulting from applied pulses were filtered at 5 kHz with a low-pass Bessel filter, and then digitized at 20 kHz. Data were acquired using an Axopatch 200B amplifier (Molecular Devices), voltage commands were generated using Pulse 8.5 software (HEKA, Germany), and ITC18 analog-to-digital interface (Instrutech, Port Washington, NY).

Protein Expression and Purification—The IFM motif of r$Na_V1.5_C$ was replaced by QQQ and the mutant gene was verified by DNA sequencing. Detailed expression and purification of rat $Na_V1.5$/QQQ was described in our previous study with modifications (Jiang et al., 2020). In brief, $Na_V1.5$/QQQ was expressed in HEK293S GnTI$^-$ cells (ATCC) with 10 μM propafenone in the medium. The protein was extracted by 1% (w/v) n-dodecyl-β-D-maltopyranoside (DDM, Anatrace) and 0.2% (w/v) cholesteryl hemisuccinate Tris salt

(CHS, Anatrace) in Buffer A containing 25 mM HEPES pH = 7.4, 150 mM NaCl, 10% glycerol, and 100 μM propafenone. After centrifugation, supernatant was agitated with anti-Flag M2-agarose resin (Sigma). Flag resin was washed in Buffer A supplemented with 0.06% glycol-diosgenin (GDN, Anatrace). The concentrated elution was loaded to Superose-6 column pre-equilibrated with buffer B containing 25 mM HEPES pH=7.4, 150 mM NaCl, 0.06% GDN, and 100 μM propafenone. Peak fractions of the first SEC were pooled and concentrated to ~ 0.5 ml, then was re-loaded to Superose-6 column pre-equilibrated with buffer C containing 25 mM imidazole pH=6.0, 150 mM NaCl, 0.006% GDN, and 100 μM propafenone. Finally, peak fractions were concentrated to 30 μl at 3.6 mg/ml.

CryoEM Grid Preparation and Data Collection—Three microliters of purified sample were applied to glow-discharged holey gold grids (UltraAuFoil, 300 mesh, R1.2/1.3), and blotted for 2.0 – 3.5 s at 100% humidity and 4 °C before being plunged frozen in liquid ethane cooled by liquid nitrogen using a FEI Mark IV Vitrobot. All data were acquired using a Titan Krios transmission electron microscope operated at 300 kV, a Gatan K2 Summit direct detector and Gatan Quantum GIF energy filter with a slit width of 20 eV. All movie stacks were automatically collected using Leginon (Suloway et al., 2005) at a nominal magnification of 130,000× with a pixel size of0.528 Å (super-resolution mode). Defocus range was set between −1.0 and −2.4 μm. The dose rate was adjusted to 8 counts/pixel/s, two separate datasets for $Na_V1.5$/QQQ were collected, 2,352 movie stacks were collected for dataset 1, each stack was exposed for 7.0 s with 35 frames with a total dose of 50 $e^-/Å^2$. 2,833 movie stacks for dataset 2, each stack was exposed for 8.4 s with 42 frames with a total dose of 60 $e^-/Å^2$.

Cryo-EM Data Processing—All the movie stacks were motion-corrected with MotionCorr2 (Zheng et al., 2017), binned 2- fold, and dose-weighted, yielding a pixel size of 1.056 Å. Defocus values of each aligned sum were estimated with Gctf (Zhang, 2016). Particle picking, 2D classification, 3D classification and 3D auto-refine was performed in RELION3.0 (Scheres, 2012). A detailed data processing diagram is presented in Figure S2. The two data sets of $Na_V1.5$/QQQ were processed separately, and the last seven frames of each stack of the second dataset were discarded to keep the same total dose of 50 $e^-/Å^2$ as dataset 1. Then the polished particles including 204,375 particles from dataset 1 and 328,465 particles from dataset 2 were combined and subjected a final round of multi-reference 3D classification. The best class containing 287,306 particles were subsequently auto-refined and sharpened in Relion 3.0. Local resolution was estimated by ResMap in Relion 3.0.

Model Building and Refinement—The structures of rat $Na_V1.5_C$ (PDB code: 6UZ0) were manually fitted into the cryo-EM density map of $Na_V1.5$/QQQ using Chimera (Pettersen et al., 2004), respectively. The models were manually checked and corrected in COOT (Emsley et al., 2010) and subsequently refined in Phenix (Adams et al., 2010). The model vs map FSC curves were calculated by Phenix.mtrage. Statistics for cryo-EM data collection and model refinement are summarized in Table S1.

Molecular Dynamics Model—The cryo-EM structures of $Na_V1.5$ (Jiang et al., 2020), $Na_V1.5$/LqhIII (Jiang et al., 2021), and $Na_V1.5$/QQQ lacking *D*I-*D*II and *D*II-*D*III linkers are composed of three chains which correspond to *D*I, *D*II, and *D*III-*D*IV. The MODELLER software (ver. 9.22) was used to insert missing residues (including the missing QQQ motif) and sidechains within the polypeptide chains, followed by quick refinement using MD with simulated annealing (Fiser and Sali, 2003).

Neutral N- and C-termini were used for the three polypeptide chains in our refined model of $Na_V1.5$. N-termini from chains *D*II and *D*III-IV were acetylated, and a neutral amino terminus (-NH_2) was used for *D*I. Neutral carboxyl groups (-COOH) were used for all C-termini. Disulfide bonds linking residues 327–342, 909–918, and 1730–1744 were included in our models of $Na_V1.5$ and $Na_V1.5$/LqhIII as they were present in the cryo-EM structure; however, no glycans were added to the protein. In the case of $Na_V1.5$/QQQ, an additional disulfide bond linking residues 281–336 was included and the 1730–1744 bond was excluded as indicated in the cryo-EM structure. For the $Na_V1.5$/LqhIII model, charged N- and C-termini were used for LqhIII and disulfide bonds linking residues 12–65, 16–37, 23–47, and 27–49 were included.

Molecular Dynamics Simulations—Molecular models of $Na_V1.5$ structures were prepared using the input generator, Membrane Builder (Jo et al., 2007; Jo et al., 2009; Lee et al., 2016; Lee et al., 2019; Wu et al., 2014) from CHARMM-GUI (Jo et al., 2009). For each model, the channel was embedded in a hydrated DMPC bilayer, with approximately 150 mM NaCl. The protein was translated and rotated for membrane embedding using the PPM server (Lomize et al., 2012). The lipid bilayer was assembled using the replacement method and solvent ions were added at random positions using a distance-based algorithm. A periodic rectangular cell with approximate dimensions of 14×14×13 nm was used, which comprised ~240,000 atoms.

The CHARMM36 all-atom force field was used in conjunction with the TIP3P water model (Best et al., 2012; Jorgensen et al., 1983; Klauda et al., 2010; MacKerell et al., 1998). Non-bonded fixes for backbone carbonyl oxygen atoms with Na^+ and lipid head groups with Na^+ were imposed (Noskov and Roux, 2008; Venable et al., 2013). For r$Na_V1.5$/QQQ, an additional non-bonded fix for guanidinium nitrogen with carboxylate oxygen was imposed (Huang et al., 2017). Electrostatic interactions were calculated using the particle-mesh Ewald algorithm (Darden, 1993; Essmann, 1995) and chemical bonds were constrained using the LINCS algorithm (Hess, 2008).

The energy of the system was minimized with protein position restraints on the backbone (4000 kJ/mol/nm^2) and side chains (2000 kJ/mol/nm^2), as well as lipid position and dihedral restraints (1000 kJ/mol/nm^2) using 5000 steps of steepest descent. The simulation systems were then pre-equilibrated using multi-step isothermal-isovolumetric (NVT) and isothermal-isobaric (NPT) conditions while decreasing the restraints at each step (see Table S2a for parameters). “Production” simulations with and without harmonic restraints on backbone heavy atoms (500 kJ/mol/nm^2) were generated with a 2 fs time integration step. The equilibration time was decided based on RMSD analyses of Cα atoms (Figure S9) and average hydration of the gate over time (Figure S10). Details on production simulations

equilibration time, and time used in analyses are indicated in Table S2b. All simulations were carried out using GROMACS version 2019.3 (http://www.gromacs.org).

Molecular Dynamics Simulation Analysis—In each snapshot of our simulations, atomic positions were translated and rotated by aligning the Cα atoms from pore transmembrane helices (S5 and S6 from all domains) of $Na_V1.5$ to the initial structure produced by CHARMM-GUI. The positions of all atoms were then centered in the xy-plane by the center of mass (CoM) of pore transmembrane helices and the z-axis by the CoM of Cα atoms from the DEKA motif in the SF. After performing the spatial transformations, the z-axis of the simulation box was used as the pore axis of $Na_V1.5$ and the transformed positions were used for subsequent analyses.

The axial distribution of water was computed by counting the number of water O atoms within a cylindrical of radius 8.5 Å centered on the pore axis. The probability distribution of water was calculated for each replica by counting the number of water molecules in uniform cylindrical slices along the pore-axis and normalizing the counts by the slice with the highest number of water molecules (solvent slice). The average and SEM of the probability distribution was computed across replicas.

Pore hydration analysis indicated a dehydrated region located at the ICAG (-2.8 nm $< z < -1.5$ nm). The number of water molecules in the gate was counted for each frame and normalized by the total number of frames to obtain the probability distribution. The average and SEM were computed across replicas.

To measure the size of the intracellular activation gate, residues at the ends of the S6 helices were selected as described (Jiang et al., 2021). The following residue number selections were used in $rNa_V1.5$: DI: 410–413, DII: 939–942, DIII: 1469–1472, and DIV: 1771–1774. The CoM of Cα-atoms from each selection was projected onto the xy-plane and the distances between opposing S6 tails were measured (d_1: DI-DIII and d_2: DII-DIV).

Analyses were performed using MDTraj (McGibbon et al., 2015) and molecular visualizations were rendered using Visual Molecular Dynamics (Humphrey et al., 1996).

QUANTIFICATION AND STATISTICAL ANALYSIS

For electrophysiological results, the data are presented as mean and standard error of the mean (SEM). Statistical significance was evaluated with Student's t-test and ANOVA. For the molecular dynamics simulations, maximum likelihood values and statistical significance were estimated by bootstrapping.

DATA AND CODE AVAILABILITY

- The cryo-EM map of the $Na_v1.5$QQQ/propafenone complex have been deposited in the Electron Microscopy Data Bank (EMDB) under accession code EMD-31519.
- The coordinates of the $Na_v1.5$QQQ/propafenone complex atomic model have been deposited in the Protein Data Bank (PDB) under accession code 7FBS.

- Any additional information required to reanalyze the data reported in this work paper is available from the Lead Contact upon request.

ADDITIONAL RESOURCES

No additional resources were generated in this work.

Supplementary Material

Refer to Web version on PubMed Central for supplementary material.

ACKNOWLEDGEMENTS

This research was supported by National Institutes of Health Research Grants R01 HL112808 and R35 NS111573 (W. A. C.), by the Howard Hughes Medical Institute (N. Z.), by the Canadian Institutes of Health Research Grant MOP130461 (R. P.), and by the Research Training Centre at the Hospital for Sick Children (R.B.). Molecular simulations were enabled by supercomputing resources and support provided by WestGrid (www.westgrid.ca), SciNet (www.scinet.ca), and Compute Canada (www.computecanada.ca). We thank Dr. Jin Li (Department of Pharmacology, University of Washington) for technical and editorial support.

References

Adams PD, Afonine PV, Bunkoczi G, Chen VB, Davis IW, Echols N, Headd JJ, Hung LW, Kapral GJ, Grosse-Kunstleve RW, et al. (2010). PHENIX: a comprehensive Python-based system for macromolecular structure solution. Acta Crystallogr D Biol Crystallogr 66, 213–221. [PubMed: 20124702]

Ahern CA, Payandeh J, Bosmans F, and Chanda B. (2016). The hitchhiker's guide to the voltage-gated sodium channel galaxy. J Gen Physiol 147, 1–24. [PubMed: 26712848]

Aryal P, Sansom MS, and Tucker SJ (2015). Hydrophobic gating in ion channels. J Mol Biol 427, 121–130. [PubMed: 25106689]

Benndorf K. (1994). Properties of single cardiac Na channels at 35 degrees C. J Gen Physiol 104, 801–820. [PubMed: 7876824]

Berendsen HJ, Postma JP, van Gunsteren WF, DiNola A, Haak JR (1984). Molecular dynamics with couipling to an external bath. J Chem Phys 81, 3684–3690.

Best RB, Zhu X, Shim J, Lopes PE, Mittal J, Feig M, and Mackerell AD Jr. (2012). Optimization of the additive CHARMM all-atom protein force field targeting improved sampling of the backbone phi, psi and side-chain chi(1) and chi(2) dihedral angles. J Chem Theory Comput 8, 3257–3273. [PubMed: 23341755]

Boiteux C, Vorobyov I, and Allen TW (2014a). Ion conduction and conformational flexibility of a bacterial voltage-gated sodium channel. Proc Natl Acad Sci U S A 111, 3454–3459. [PubMed: 24550503]

Boiteux C, Vorobyov I, French RJ, French C, Yarov-Yarovoy V, and Allen TW (2014b). Local anesthetic and antiepileptic drug access and binding to a bacterial voltage-gated sodium channel. Proc Natl Acad Sci U S A 111, 13057–13062. [PubMed: 25136136]

Capes DL, Goldschen-Ohm MP, Arcisio-Miranda M, Bezanilla F, and Chanda B. (2013). Domain IV voltage-sensor movement is both sufficient and rate limiting for fast inactivation in sodium channels. J Gen Physiol 142, 101–112. [PubMed: 23858005]

Catterall WA (2000). From ionic currents to molecular mechanisms: The structure and function of voltage-gated sodium channels. Neuron 26, 13–25. [PubMed: 10798388]

Catterall WA, Lenaeus MJ, and Gamal El-Din TM (2020). Structure and pharmacology of voltage-gated sodium and calcium channels. Annu Rev Pharmacol Toxicol 60, 133–154. [PubMed: 31537174]

Catterall WA, and Maier SKG (2015). Voltage-gated sodium channels and the electrical excitability of the heart. In Cardiac Electrophysiology: From Bench to Bedside, Zipes DJ, and Jalife J, eds. (Saunders/Elsevier).

Chanda B, and Bezanilla F. (2002). Tracking voltage-dependent conformational changes in skeletal muscle sodium channel during activation. J Gen Physiol 120, 629–645. [PubMed: 12407076]

Clairfeuille T, Cloake A, Infield DT, Llongueras JP, Arthur CP, Li ZR, Jian Y, Martin-Eauclaire MF, Bougis PE, Ciferri C., et al. (2019). Structural basis of alpha-scorpion toxin action on Nav channels. Science.

Clancy CE, and Kass RS (2005). Inherited and acquired vulnerability to ventricular arrhythmias: cardiac Na+ and K+ channels. Physiol Rev 85, 33–47. [PubMed: 15618477]

Darden T, York D, Pedersen L. (1993). Particle mesh Ewald: An N-log(N) method for Ewald sums in large systems. J Chem Phys 98, 10089–10092.

Eaholtz G, Scheuer T, and Catterall WA (1994). Restoration of inactivation and block of open sodium channels by an inactivation gate peptide. Neuron 12, 1041–1048. [PubMed: 8185942]

Emsley P, Lohkamp B, Scott WG, and Cowtan K. (2010). Features and development of Coot. Acta Crystallogr D Biol Crystallogr 66, 486–501. [PubMed: 20383002]

Essmann UP, L., Berkowitz ML, Darden T, Lee H, Pedersen L. (1995). A smooth particle mesh Ewald method. J Chem Phys 103, 8577–8593.

Fiser A, and Sali A. (2003). Modeller: generation and refinement of homology-based protein structure models. Methods Enzymol 374, 461–491. [PubMed: 14696385]

Gamal El-Din TM, Lenaeus MJ, Zheng N, and Catterall WA (2018). Fenestrations control resting-state block of a voltage-gated sodium channel. Proc Natl Acad Sci U S A 115, 13111–13116. [PubMed: 30518562]

Goldin AL (2003). Mechanisms of sodium channel inactivation. Curr Opin Neurobiol 13, 284–290. [PubMed: 12850212]

Hess B. (2008). P-LINCS: A Parallel Linear Constraint Solver for Molecular Simulation. J Chem Theory Comput 4, 116–122. [PubMed: 26619985]

Hille B. (1977). Local anesthetics: hydrophilic and hydrophobic pathways for the drug-receptor reaction. JGenPhysiol 69, 497–515.

Hille B. (2001). Ionic Channels of Excitable Membranes, 3rd Ed (Sunderland, MA: Sinauer Associates Inc.).

Hondeghem LM, and Katzung BG (1984). Antiarrhythmic agents: The modulated receptor mechanism of action of sodium and calcium channel blocking drugs. Annu Rev Pharmacol Toxicol 24, 387–423. [PubMed: 6203481]

Hoover WG (1985). Canonical dynamics: Equilibrium phase-space distributions. Phys Rev A Gen Phys 31, 1695–1697. [PubMed: 9895674]

Huang J, Rauscher S, Nawrocki G, Ran T, Feig M, de Groot BL, Grubmuller H, and MacKerell AD Jr. (2017). CHARMM36m: an improved force field for folded and intrinsically disordered proteins. Nat Methods 14, 71–73. [PubMed: 27819658]

Humphrey W, Dalke A, and Schulten K. (1996). VMD: visual molecular dynamics. J Mol Graph 14, 33–38, 27–38. [PubMed: 8744570]

Jiang D, Shi H, Tonggu L, Gamal El-Din TM, Lenaeus MJ, Zhao Y, Yoshioka C, Zheng N, and Catterall WA (2020). Structure of the cardiac sodium channel. Cell 180, 122–134. [PubMed: 31866066]

Jiang D, Tonggu L, Gamal El-Din TM, Banh R, Pomes R, Zheng N, and Catterall WA (2021). Structural basis for voltage-sensor trapping of the cardiac sodium channel by a deathstalker scorpion toxin. Nat Commun 12, 128. [PubMed: 33397917]

Jo S, Kim T, and Im W. (2007). Automated builder and database of protein/membrane complexes for molecular dynamics simulations. PLoS One 2, e880. [PubMed: 17849009]

Jo S, Lim JB, Klauda JB, and Im W. (2009). CHARMM-GUI Membrane Builder for mixed bilayers and its application to yeast membranes. Biophys J 97, 50–58. [PubMed: 19580743]

Jorgensen WL, Chandrasekhar J, Madura JD, Impey RW, and Klein ML (1983). Comparison of Simple Potential Functions for Simulating Liquid Water. Journal of Chemical Physics 79, 926–935.

Karlin A, and Akabas MH (1998). Substituted-cysteine accessibility method. Methods Enzymol 293, 123–145. [PubMed: 9711606]

Kellenberger S, Scheuer T, and Catterall WA (1996). Movement of the Na^+ channel inactivation gate during inactivation. J Biol Chem 271, 30971–30979. [PubMed: 8940085]

Kellenberger S, West JW, Catterall WA, and Scheuer T. (1997a). Molecular analysis of potential hinge residues in the inactivation gate of brain type IIA Na^+ channels. JGenPhysiol 19, 607–617.

Kellenberger S, West JW, Scheuer T, and Catterall WA (1997b). Molecular analysis of the putative inactivation particle in the inactivation gate of brain type IIA Na^+ channels. JGenPhysiol 109, 589–605.

Klauda JB, Venable RM, Freites JA, O'Connor JW, Tobias DJ, Mondragon-Ramirez C, Vorobyov I, MacKerell AD Jr., and Pastor RW (2010). Update of the CHARMM all-atom additive force field for lipids: validation on six lipid types. J Phys Chem B 114, 7830–7843. [PubMed: 20496934]

Kohlhardt M, and Fichtner H. (1988). Block of single cardiac Na+ channels by antiarrhythmic drugs: the effect of amiodarone, propafenone and diprafenone. J Membr Biol 102, 105–119. [PubMed: 2458471]

Lee J, Cheng X, Swails JM, Yeom MS, Eastman PK, Lemkul JA, Wei S, Buckner J, Jeong JC, Qi Y., et al. (2016). CHARMM-GUI Input Generator for NAMD, GROMACS, AMBER, OpenMM, and CHARMM/OpenMM Simulations Using the CHARMM36 Additive Force Field. J Chem Theory Comput 12, 405–413. [PubMed: 26631602]

Lee J, Patel DS, Stahle J, Park SJ, Kern NR, Kim S, Lee J, Cheng X, Valvano MA, Holst O., et al. (2019). CHARMM-GUI Membrane Builder for Complex Biological Membrane Simulations with Glycolipids and Lipoglycans. J Chem Theory Comput 15, 775–786. [PubMed: 30525595]

Lenaeus MJ, Gamal El-Din TM, Ing C, Ramanadane K, Pomes R, Zheng N, and Catterall WA (2017). Structures of closed and open states of a voltage-gated sodium channel. Proc Natl Acad Sci U S A 114, E3051–E3060. [PubMed: 28348242]

Lerche H, Peter W, Fleischhauer R, Pika-Hartlaub U, Malina T, Mitrovic N, and Lehmann-Horn F. (1997). Role in fast inactivation of the IV/S4-S5 loop of the human muscle Na+ channel probed by cysteine mutagenesis. JPhysiol(Lond) 505, 345–352. [PubMed: 9423178]

Lomize MA, Pogozheva ID, Joo H, Mosberg HI, and Lomize AL (2012). OPM database and PPM web server: resources for positioning of proteins in membranes. Nucleic Acids Res 40, D370–376. [PubMed: 21890895]

MacKerell AD, Bashford D, Bellott M, Dunbrack RL, Evanseck JD, Field MJ, Fischer S, Gao J, Guo H, Ha S., et al. (1998). All-atom empirical potential for molecular modeling and dynamics studies of proteins. J Phys Chem B 102, 3586–3616. [PubMed: 24889800]

McGibbon RT, Beauchamp KA, Harrigan MP, Klein C, Swails JM, Hernandez CX, Schwantes CR, Wang LP, Lane TJ, and Pande VS (2015). MDTraj: A Modern Open Library for the Analysis of Molecular Dynamics Trajectories. Biophys J 109, 1528–1532. [PubMed: 26488642]

McPhee JC, Ragsdale D, Scheuer T, and Catterall WA (1998). A critical role for the S4-S5 intracellular loop in domain IV of the sodium channel alpha subunit in fast inactivation. J Biol Chem 273, 1121–1129. [PubMed: 9422778]

McPhee JC, Ragsdale DS, Scheuer T, and Catterall WA (1994). A mutation in segment IVS6 disrupts fast inactivation of sodium channels. Proc Natl Acad Sci U S A 91, 12346–12350. [PubMed: 7991630]

McPhee JC, Ragsdale DS, Scheuer T, and Catterall WA (1995). A critical role for transmembrane segment IVS6 of the sodium channel alpha subunit in fast inactivation. J Biol Chem 270, 12025–12034. [PubMed: 7744852]

Neale C, Chakrabarti N, Pomorski P, Pai EF, and Pomes R. (2015). Hydrophobic gating of ion permeation in magnesium channel CorA. PLoS Comput Biol 11, e1004303. [PubMed: 26181442]

Nguyen PT, DeMarco KR, Vorobyov I, Clancy CE, and Yarov-Yarovoy V. (2019). Structural basis for antiarrhythmic drug interactions with the human cardiac sodium channel. Proc Natl Acad Sci U S A 116, 2945–2954. [PubMed: 30728299]

Noble D. (1984). The surprising heart: a review of recent progress in cardiac electrophysiology. J Physiol 353, 1–50. [PubMed: 6090637]

Nose S. (2006a). A molecular dynamics method for simulations in the canonical ensemble. Mol Phys 52, 255–268.

Nose S, Klein M. (2006b). Constant pressure under molecular dynamics for molecular systems Mol Phys 50, 1055–1076.

Noskov SY, and Roux B. (2008). Control of ion selectivity in LeuT: two Na+ binding sites with two different mechanisms. J Mol Biol 377, 804–818. [PubMed: 18280500]

Pan X, Li Z, Huang X, Huang G, Gao S, Shen H, Liu L, Lei J, and Yan N. (2019). Molecular basis for pore blockade of human Na^+ channel NaV1.2 by the mu-conotoxin KIIIA. Science 363, 1309–1313. [PubMed: 30765605]

Pan X, Li Z, Zhou Q, Shen H, Wu K, Huang X, Chen J, Zhang J, Zhu X, Lei J., et al. (2018). Structure of the human voltage-gated sodium channel NaV1.4 in complex with beta1. Science 362, pii: eaau2486. [PubMed: 30190309]

Parrinello M, Rahman A. (1980). Crystal structure and pair potentials:a molecular dymanics study. Phys Rev Lett 45, 1196–1199.

Payandeh J, Scheuer T, Zheng N, and Catterall WA (2011). The crystal structure of a voltage-gated sodium channel. Nature 475, 353–358. [PubMed: 21743477]

Pettersen EF, Goddard TD, Huang CC, Couch GS, Greenblatt DM, Meng EC, and Ferrin TE (2004). UCSF Chimera--a visualization system for exploratory research and analysis. J Comput Chem 25, 1605–1612. [PubMed: 15264254]

Pless SA, Galpin JD, Frankel A, and Ahern CA (2011). Molecular basis for class Ib anti-arrhythmic inhibition of cardiac sodium channels. Nat Commun 2, 351. [PubMed: 21673672]

Ragsdale DS, McPhee JC, Scheuer T, and Catterall WA (1994). Molecular determinants of state-dependent block of sodium channels by local anesthetics. Science 265, 1724–1728. [PubMed: 8085162]

Rogers JC, Qu Y, Tanada TN, Scheuer T, and Catterall WA (1996). Molecular determinants of high affinity binding of alpha-scorpion toxin and sea anemone toxin in the S3-S4 extracellular loop in domain IV of the Na^+ channel alpha subunit. JBiolChem 271, 15950–15962.

Rohl CA, Boeckman FA, Baker C, Scheuer T, Catterall WA, and Klevit RE (1999). Solution structure of the sodium channel inactivation gate. Biochemistry 38, 855–861. [PubMed: 9893979]

Scheres SH (2012). RELION: implementation of a Bayesian approach to cryo-EM structure determination. J Struct Biol 180, 519–530. [PubMed: 23000701]

Shen H, Liu D, Wu K, Lei J, and Yan N. (2019). Structures of human NaV1.7 channel in complex with auxiliary subunits and animal toxins. Science 363, 1303–1308. [PubMed: 30765606]

Smith MR, and Goldin AL (1997). Interaction between the sodium channel inactivation linker and domain III S4-S5. BiophysJ 73, 1885–1895. [PubMed: 9336184]

Stuhmer W, Conti F, Suzuki H, Wang X, Noda M, Yahadi N, Kubo H, and Numa S. (1989). Structural parts involved in activation and inactivation of the sodium channel. Nature 339, 597–603. [PubMed: 2543931]

Suloway C, Pulokas J, Fellmann D, Cheng A, Guerra F, Quispe J, Stagg S, Potter CS, and Carragher B. (2005). Automated molecular microscopy: the new Leginon system. J Struct Biol 151, 41–60. [PubMed: 15890530]

Vassilev P, Scheuer T, and Catterall WA (1989). Inhibition of inactivation of single sodium channels by a site-directed antibody. ProcNatlAcadSciUSA 86, 8147–8151.

Vassilev PM, Scheuer T, and Catterall WA (1988). Identification of an intracellular peptide segment involved in sodium channel inactivation. Science 241, 1658–1661. [PubMed: 2458625]

Venable RM, Luo Y, Gawrisch K, Roux B, and Pastor RW (2013). Simulations of anionic lipid membranes: development of interaction-specific ion parameters and validation using NMR data. J Phys Chem B 117, 10183–10192. [PubMed: 23924441]

Weiss RE, and Horn R. (1986). Functional differences between two classes of sodium channels in developing rat skeletal muscle. Science 233, 361–364. [PubMed: 2425432]

West JW, Patton DE, Scheuer T, Wang Y, Goldin AL, and Catterall WA (1992). A cluster of hydrophobic amino acid residues required for fast Na^+ channel inactivation. Proc Natl Acad Sci U S A 89, 10910–10914. [PubMed: 1332060]

Wisedchaisri G, Tonggu L, McCord E, Gamal El-Din TM, Wang L, Zheng N, and Catterall WA (2019). Resting-state structure and gating mechanism of a voltage-gated sodium channel. Cell 178, 993–1003. [PubMed: 31353218]

Wu EL, Cheng X, Jo S, Rui H, Song KC, Davila-Contreras EM, Qi Y, Lee J, Monje-Galvan V, Venable RM, et al. (2014). CHARMM-GUI Membrane Builder toward realistic biological membrane simulations. J Comput Chem 35, 1997–2004. [PubMed: 25130509]

Zhang K. (2016). Gctf: Real-time CTF determination and correction. J Struct Biol 193, 1–12. [PubMed: 26592709]

Zheng SQ, Palovcak E, Armache JP, Verba KA, Cheng Y, and Agard DA (2017). MotionCor2: anisotropic correction of beam-induced motion for improved cryo-electron microscopy. Nat Methods 14, 331–332. [PubMed: 28250466]

Highlights

- Mutation of the fast inactivation gate IFM motif allows stable opening of the pore
- The intracellular activation gate opens to ~10Å, sufficient to conduct hydrated Na^+
- Molecular dynamics analysis reveals Na^+ conductance at about physiological rates
- The antiarrhythmic drug propafenone binds the open state tightly and blocks the pore

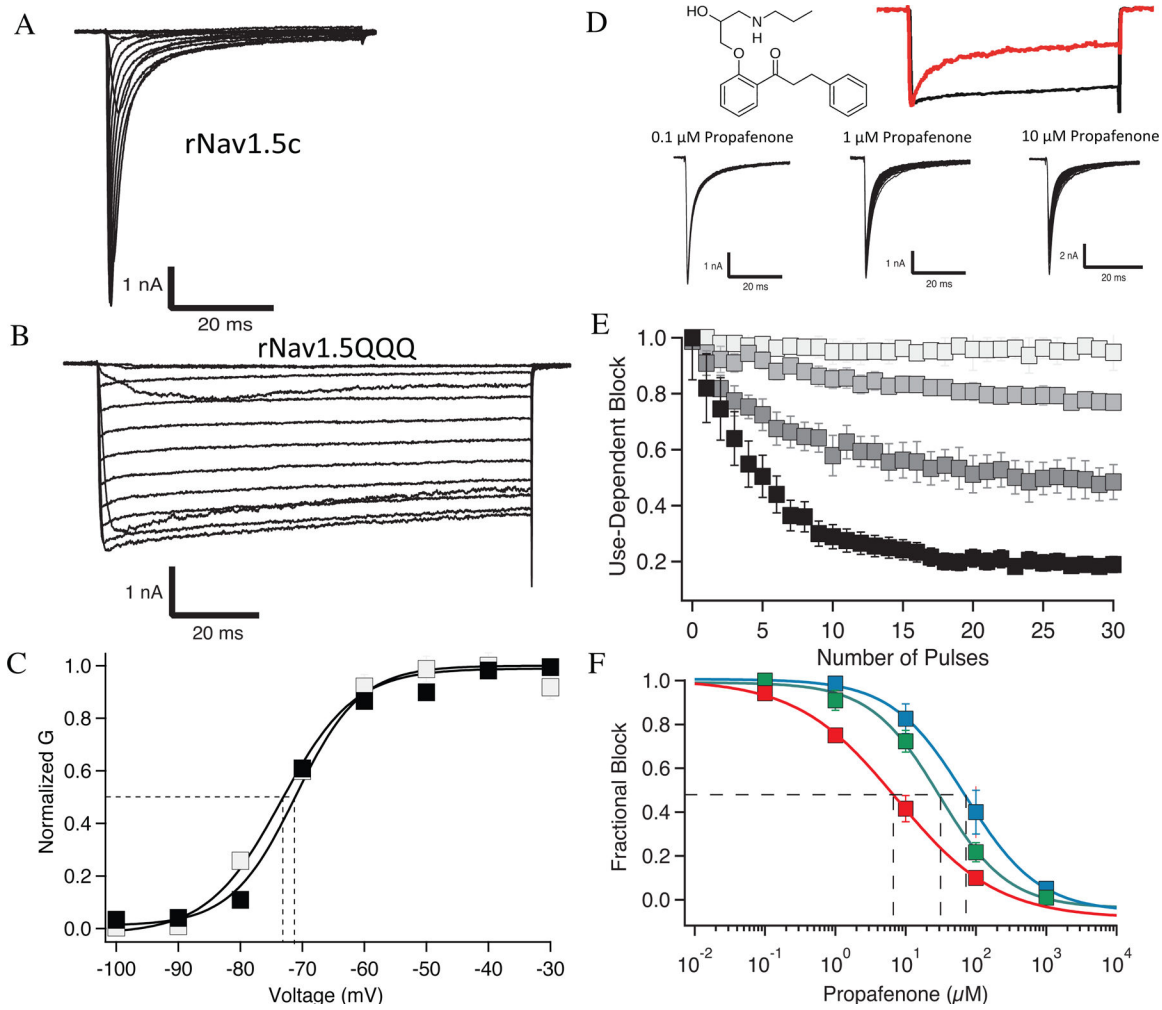

Figure 1. Capturing $Na_V1.5$/QQQ in the Open State

(A) A family of sodium currents conducted by $rNa_V1.5c$.

(B) A family of sodium currents conducted by $Na_V1.5$/QQQ.

(C) Conductance/voltage (G/V) curves for $Na_V1.5_C$ (black), and $Na_V1.5$/QQQ (white). HEK cells expressing the indicated sodium channel constructs were held at −120 mV, and 100-ms pulses were applied in 10 mV increments from −120 mV to +60 mV. Each point is an average of 4–6 cells. The lines through the curves are fits of Boltzmann relationships with values of V_a = −73.3 ± 3.5 mV and k = 6.0 ± 2.8 mV for the $Na_V1.5c$ and V_a = −75.1 ± 1.1 mV and k = 6.1 ± 1.2 mV for $Na_V1.5$/QQQ.

(D) Top. Chemical structure of propafenone. Sodium current conducted by $Na_V1.5$/QQQ without (black) and with (red) 10 μM propafenone. Bottom. Frequency-dependent block by the indicated concentrations of propafenone.

(E) Use-dependent block of $Na_V1.5$/QQQ currents in 30 repetitive pulses from a holding potential of −120 mV to a test pulse of 0 mV. Shades of gray indicate 0, 1, 10, and 100 μM propafenone.

(F) Comparison of use-dependent block under different stimulus conditions: at the holding potential of −120 mV with no depolarizing stimuli (blue; IC_{50}= 70 ± 7.5 μM); following a

train of 50-ms depolarizations to 0 mV at 0.2 Hz (green, IC_{50}= 26 ± 5.6 μM); and following a train of 50-ms depolarizations to 0 mV at 1 Hz (red, IC_{50}= 6 ± 1.7 μM). Each point is the mean of 6–10 cells.

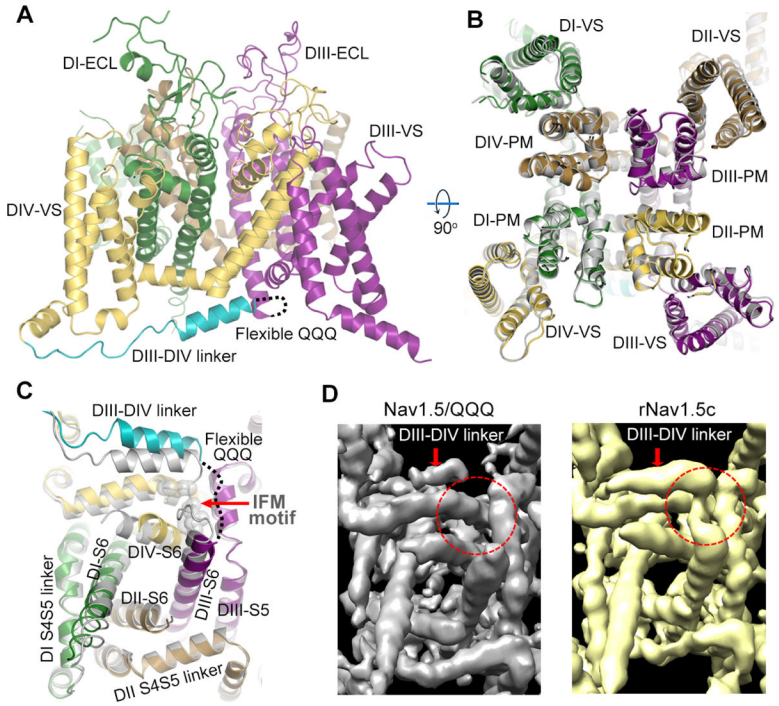

Figure 2. Releasing the Fast Inactivation Gate of $Na_V1.5$/QQQ

(A) Side view of $Na_V1.5$/QQQ. Domains *D*I, *D*II, *D*III, *D*IV and *D*III-*D*IV linker of $Na_V1.5$/QQQ are colored green, brown, purple, gold and cyan, respectively. The same color code applied for $Na_V1.5$/QQQ throughout the manuscript unless specified. Black dashed curve indicates the flexible QQQ region.

(B) Top view of $Na_V1.5$/QQQ superimposed on $rNa_V1.5c$ (Colored in gray).

(C) Bottom view of $Na_V1.5$/QQQ superimposed on $rNa_V1.5c$ (Colored in gray). The label 'IFM motif' indicates the position of the bound IFM sequence of the fast inactivation gate of $rNa_V1.5c$. The label 'Flexible QQQ' and the dotted line indicate the loss of cryo-EM density for the IFM segments of the fast inactivation gate in $Na_V1.5$/QQQ.

(D) Resolution low-passed cryo-EM map viewed from intracellular side for $Na_V1.5$/QQQ (gray) and $rNa_V1.5_C$ (yellow), respectively. The red arrows indicate the position of *D*III-*D*IV linker helices, and the red dashed circles show the IFM binding pocket. Note the loss of cryo-EM density for the flexible QQQ motif in the fast inactivation gate.

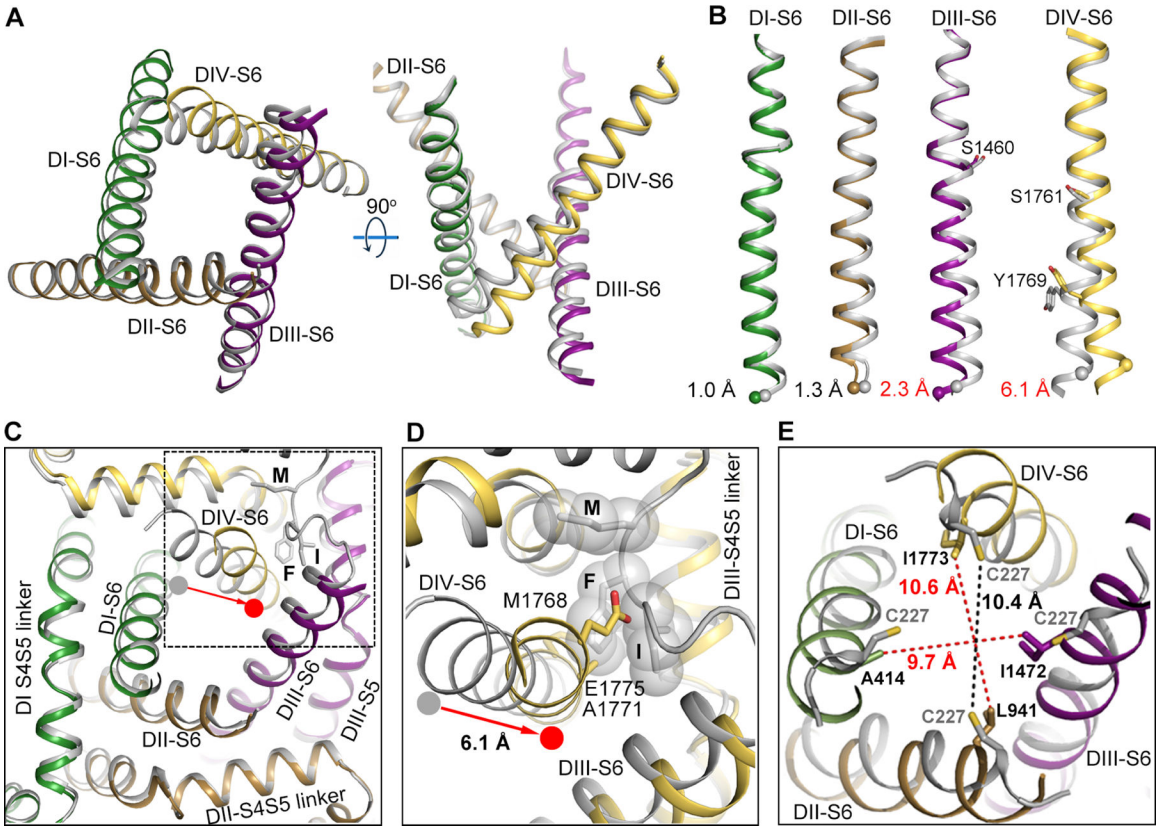

Figure 3. Structure of the Open Activation Gate

(A) Comparison of S6 segments of $Na_V1.5$/QQQ with that of $Na_V1.5_C$ (gray).

(B) Conformational change of the S6 segment in each domain as measured between Cα atoms of Ala423, Ser943, Lys1479 and Glu1775 for *DI*-S6, *DII*-S6, *DIII*-S6 and *DIV*-S6, respectively.

(C) Activation gate alignment of $rNa_V1.5_C$ (grey), $Na_V1.5$/LqhIII (orange), and $Na_V1.5$/QQQ (red). Gray, orange, and red solid circles represent positions of the *DIV*-S6 at the activation gates. Red arrows indicate conformational shifts of S6 segments.

(D) Close-up view of the area in the black dashed square in panel **C**.

(E) Comparison of the activation gate of $Na_V1.5$/QQQ with open Na_VAb (gray). Black dashed line shows the diameter of the Na_VAb (PDB code: 5VB8) activation gate calculated from the end of C227 side chain. Red dashed lines show the diameter of $Na_V1.5$/QQQ gate between *D*I-*D*III and *D*II-*D*IV.

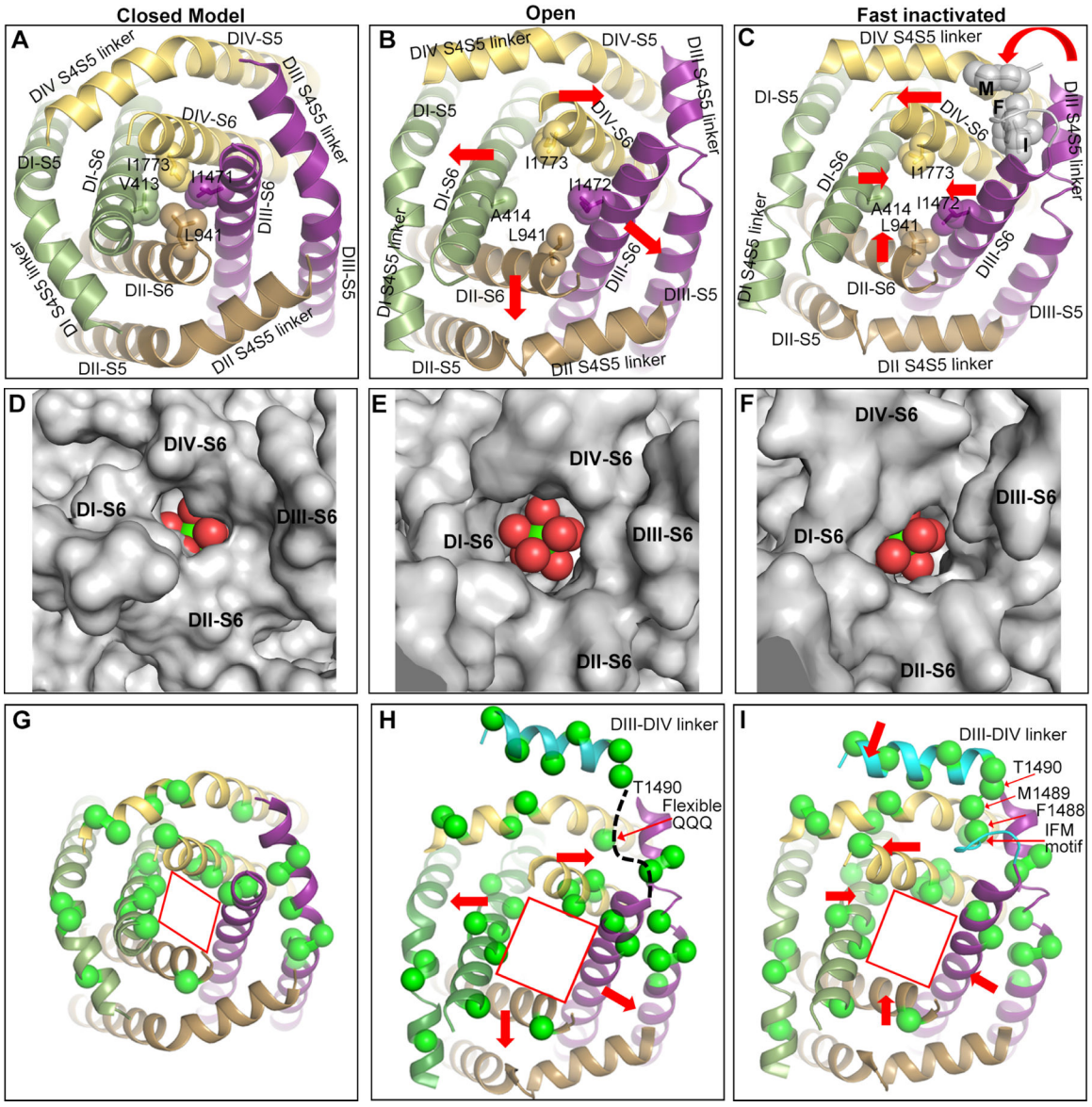

Figure 4. Closed, Open and Inactivated Conformations of the Activation Gate and the Locations of Arrhythmia Mutations

(A) Closed activation gate of $Na_V1.5$ generated by MODELLER based on the resting-state structure of Na_VAb (PDB code: 6P6W), sealed by a square of hydrophobic side chains of Ile217. **(B)** Open activation gate of $Na_V1.5$/QQQ. Red arrows indicate the directions of movement of S6 segments compared to the resting state.

(C) Partially open but nonconductive activation gate of $rNa_V1.5_C$ in the inactivated state. Red arrows indicate the directions of movement of the S6 segments compared to the open state.

(D-F) Structures from panels A-C are shown in spacefilling surface representation with hydrated Na^+ placed in the central cavity behind the activation gate. Red and green spheres represent water and Na^+, respectively. Van der Waals distances measured across the orifice of the activation gate are: 4.3 Å (*D*I-*D*III) x 2.8 Å (*D*II-*D*IV) for the resting/closed state;

6.9 Å (*D*I-*D*III) x 5.0 Å (*D*II-*D*IV) for the inactivated state; and 7.3 Å (*D*I-*D*III) x 8.2 Å (*D*II-*D*IV) for the $Na_V1.5$/QQQ open state structure.

(**G-I)** Structures from panels **A-C** with the locations of arrhythmia mutations causing LQT-3 overlaid as green spheres.

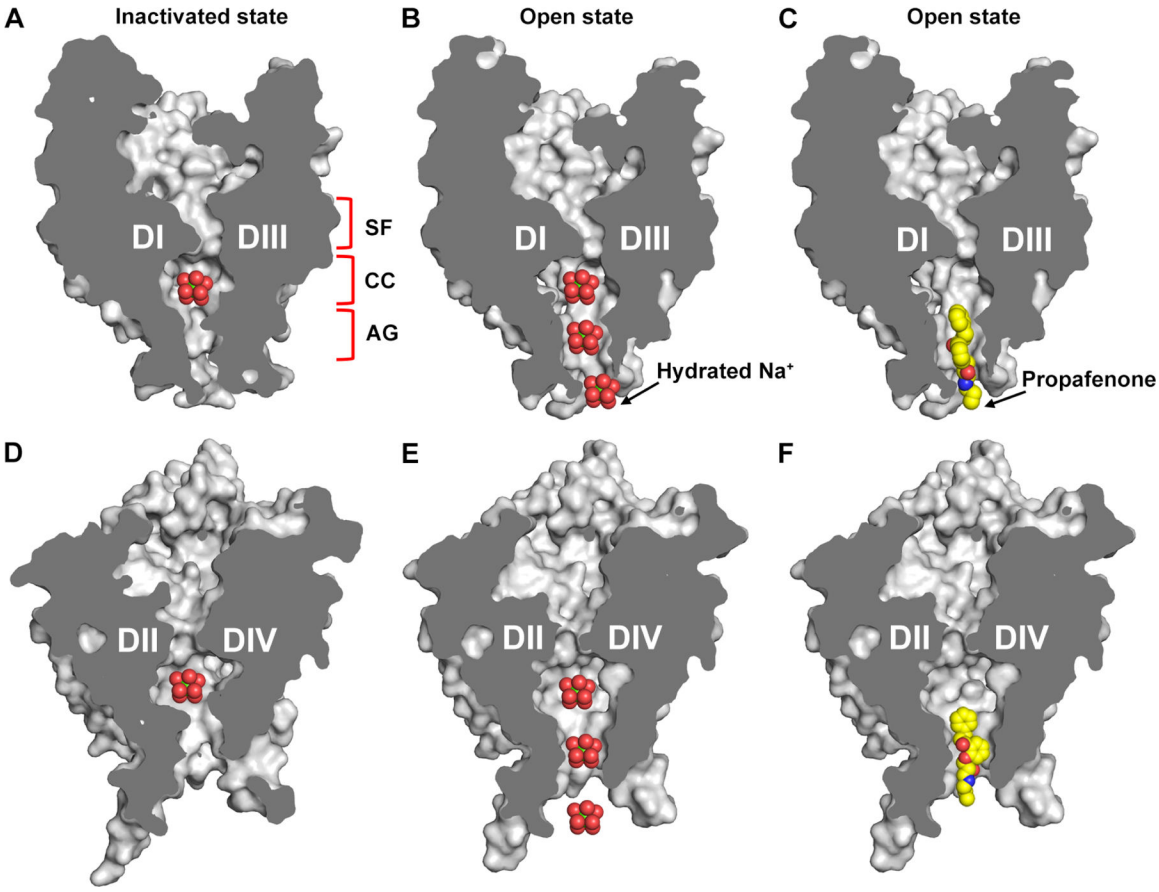

Figure 5. Hydrated Na^+ and Propafenone in the Open Activation Gate

(A) Sliced side-view of the pore module of the inactivated state shown in surface representation. The conducting pore lined by *DI* and *DIII* is composed of the selectivity filter (SF), central cavity (CC) and activation gate (AG). Hydrated Na^+ is trapped inside the central cavity.

(B) Sliced side-view of the pore module of the open state shown in surface representation. Hydrated Na^+ is permeable through the activation gate.

(C) Sliced side-view of the pore module of the open state shown in surface representation. Propafenone is illustrated in the open activation gate, indicating that it would be permeable through this open activation gate structure.

(D-F) Sliced side-view from panels **A-C** in surface representation showing the pore lined by *DII* and *DIV*.

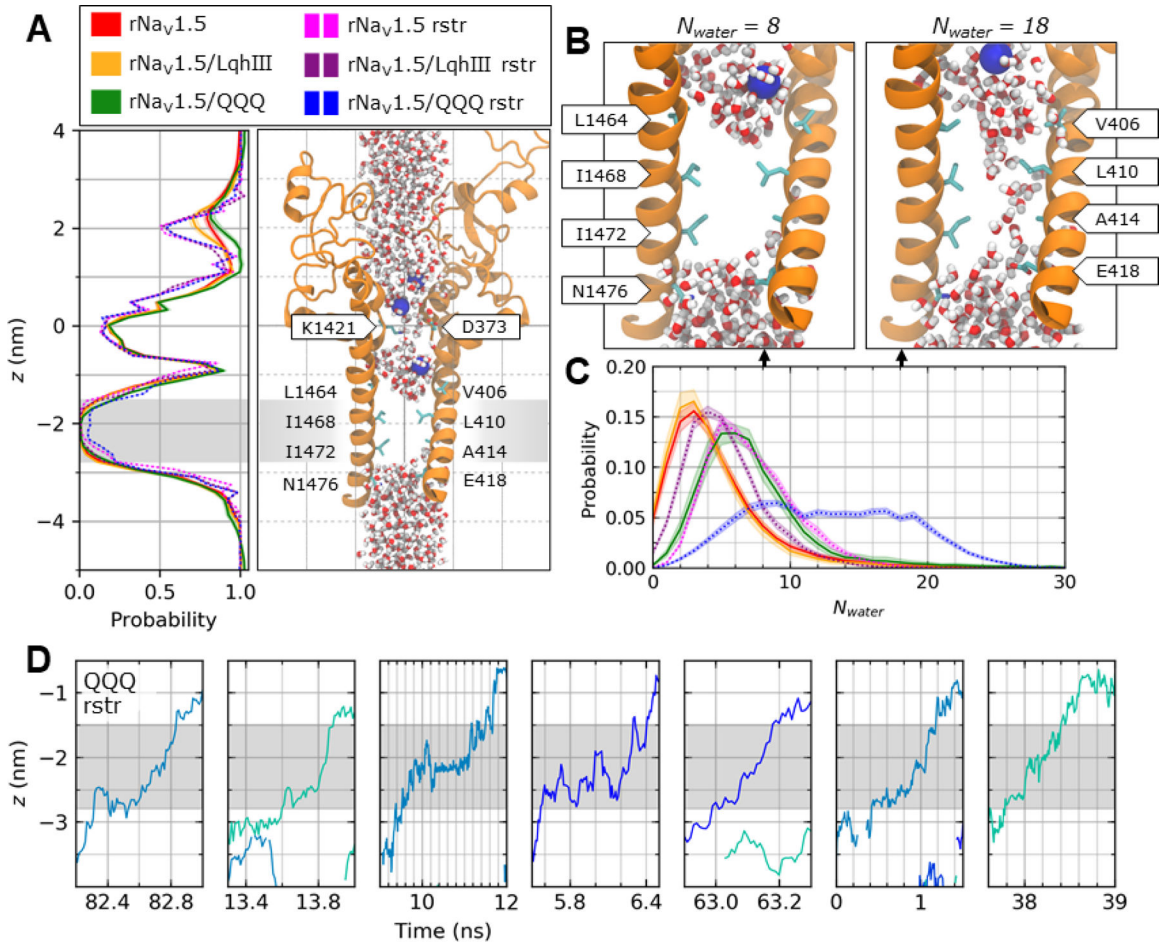

Figure 6. Molecular Dynamics Analysis of Pore Hydration and Na^+ Permeation

(A) (Left) Average hydration along the pore axis (*z*) in unrestrained simulations of $Na_V1.5$ (solid red line), $Na_V1.5$/LqhIII (solid orange line), and $Na_V1.5$/QQQ (solid green line); and restrained (rstr) simulations of $Na_V1.5$ (dotted magenta line), $Na_V1.5$/LqhIII (dotted purple line), and $Na_V1.5$/QQQ (dotted blue line). The intracellular activation gate region (grey shaded region; -2.8 nm < *z* < -1.5 nm) is dehydrated in all systems except for restrained simulations of $rNa_V1.5$/QQQ. Line shading corresponds to the standard error of the mean (SEM). (Right) Side-view of $Na_V1.5$ (orange ribbons; only *D*I and *D*III are shown for clarity) with pore-facing side chains (cyan licorice), Na^+ (blue spheres), and water molecules (red and white licorice) shown in a cylindrical radius of 8.5 Å.

(B) Side view of the $Na_V1.5$/QQQ gate containing *Nwater* = 8 (left) or 18 (right).

(C) Probability distribution of *Nwater* in the activation gate. Shading represents the SEM.

(D) Time series of Na^+ positions along *z* from seven restrained simulations of $rNa_V1.5$/QQQ where spontaneous permeation of Na^+ across the gate was observed. Breaks are observed when Na^+ is outside the cylinder. X-axis gridlines are shown every 0.2 ns.

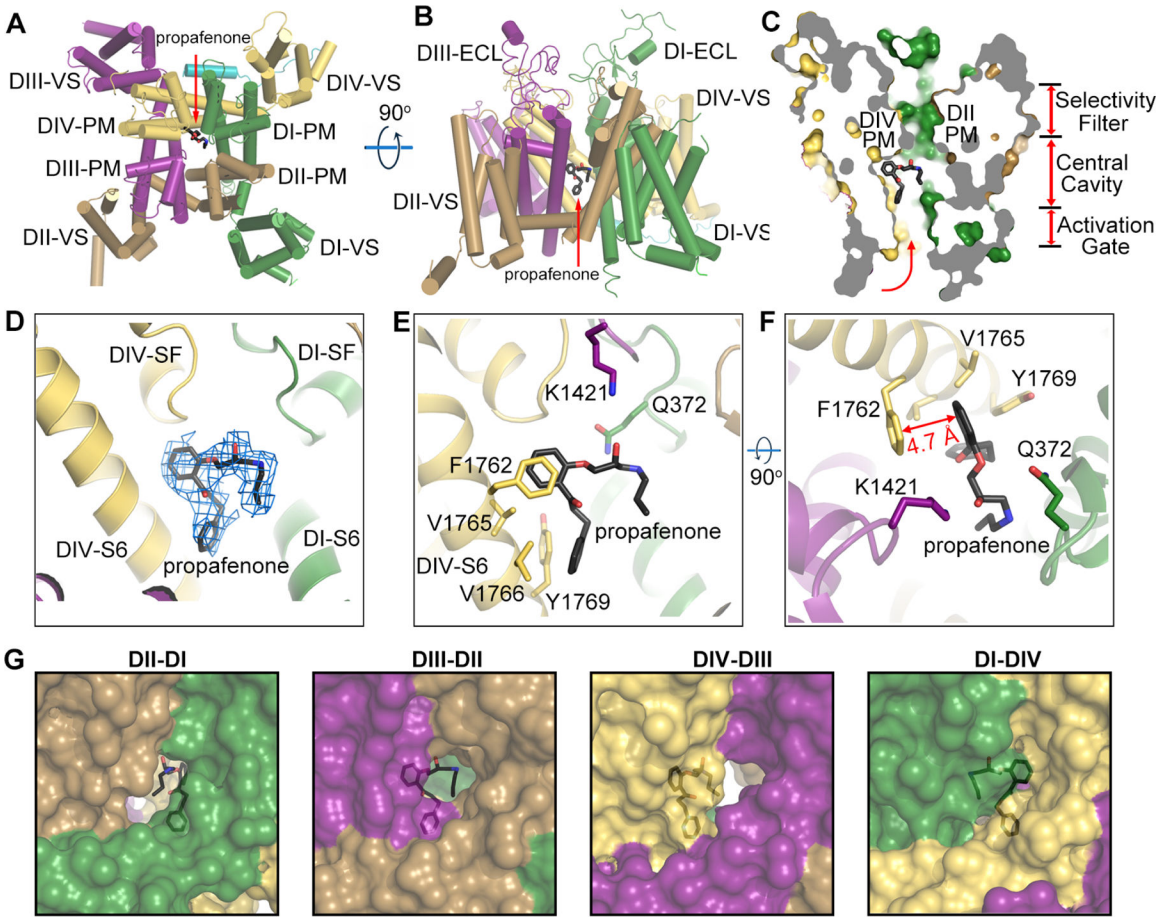

Figure 7. Structural Basis for Open State Block by Propafenone

(A and B) Top view and side view of the binding site of propafenone.

(C) Cut-open surface presentation of bound propafenone.

(D) Cryo-EM density shown in blue mesh for propafenone (black sticks) contoured at 3σ.

(E and F) Detailed side and top views of the binding site of propafenone. The key drug-binding residues F1762 and Y1769 are illustrated in yellow sticks.

(G) Surface presentation of the four fenestrations of neighboring domains. Propafenone is shown in black sticks bound in its receptor site in the pore within the channel structure.

KEY RESOURCES TABLE

REAGENT or RESOURCE	SOURCE	IDENTIFIER
Antibodies		
Mouse Monoclonal Anti-FLAG M2 Antibody	Sigma-Aldrich	Cat# F1804
Bacterial and Virus Strains		
E. coli GC10	Genesee Scientific	Cat# 42–661
E. coli DH10Bac	ThermoFisher Scientific	Cat# 10361–012
Chemicals, Peptides, and Recombinant Proteins		
n-Dodecyl-β-D-Maltoside (DDM)	Anatrace	Cat# D310
Glyco-diosgenin (GDN)	Anatrace	Cat# GDN101
Propafenone	Sigma-Aldrich	Cat# 1570304
Cholesteryl Hemisuccinate Tris Salt (CHS)	Anatrace	Cat# CH210
Anti-FLAG M2 Affinity Gel	Millipore Sigma	Cat# A2220
FLAG peptide DYKDDDDK	Bio Basic	N/A
Deposited Data		
Coordinates and Structure Factors of rNa$_v$1.5/QQQ	This study	PDB: 7FBS
Cryo-EM Map of rNa$_v$1.5/QQQ	This study	EMDB: EMD-31519
Experimental Models: Cell Lines		
Spodoptera frugiperda (Sf9)	Life Technologies	B825–01
HEK293S GnTI$^-$	ATCC	CRL-3022
Recombinant DNA		
pEG-BacMam rNa$_v$1.5/QQQ-eGFP-Flag	This study	N/A
Software and Algorithms		
Coot 0.8.9.1	MRC	https://www2.mrc-lmb.cam.ac.uk/personal/pemsley/coot
Leginon 3.3	NRAMM	http://leginon.org
MotionCor2	UCSF	https://msg.ucsf.edu/software
Gctf	MRC	https://www.mrc-lmb.cam.ac.uk/kzhang
Relion 3.0 beta	MRC	https://www2.mrc-lmb.cam.ac.uk/relion
CisTEM 1.0.0-beta	https://cistem.org	https://cistem.org
MonoRes	Scipion	http://scipion.cnb.csic.es/m/myresmap
Chimera 1.11.2	UCSF	https://www.cgl.ucsf.edu/chimera
Phenix 1.14–3260	https://www.phenix-online.org	https://www.phenix-online.org
MODELLER	UCSF	https://salilab.org/modeller/
MOLE*Online*	ELIXIR-CZ	https://mole.upol.cz
Pymol 1.7.2	Schrödinger	https://pymol.org